1

Advanced Wide-Field Fluorescent Microscopy for Biomedicine

Chong Chen and Hui Li

Suzhou Institute of Biomedical Engineering and Technology, Chinese Academy of Science, Suzhou 215163, China

1.1 Introduction

Life was assembled from molecules, subcellular organelles, cells, tissues, organs, to the whole organism in totally different ways. The assembly at each level has its own structure, dynamics, and functions, making for such a complex and beautiful living world. To study such complex structures, as nobel prize winner Feynmann said, "It is very easy to understand many of these fundamental biology questions: you just look at the things." However, different imaging tools need to be developed for different purposes to look at the various biological objects, with a scale from nanometers to centimeters.

Optical microscopy plays the most important role in inspecting the microscale biological world among all the imaging tools. Although optical microscopy has been invented for more than 300 years, we have witnessed significant improvement in the optical microscope technique in the last 30 years. These improvements mostly fall into two aspects: sample labeling technique and different imaging modalities.

Image contrast is the first factor to be concerned with for optical imaging. By now, fluorescent imaging has provided the highest contrast due to the filtering out of excitation light. Organic dyes, quantum dots, and fluorescent protein are the three most widely used fluorescent labeling agents. Fluorescent proteins, which won the novel prize for chemistry in 2008, provide a genetic way for labeling so that fluorescent imaging with live cells, organelles, and even live animals becomes possible.

High-end microscopes fall into two categories: widefield microscopes and point scanning microscopes (Figure 1.1). A wide-field microscope takes imaging by a camera and usually has high speed and high photon efficiency. Typical examples are the Tirf-microscope, structured illumination microscope, and single-molecule localization super-resolution microscope. The point-scanning microscope takes imaging by fast scanning the excitation laser beam or sample, usually at a lower speed but with higher axial sectioning capability. Typical examples include laser scanning confocal microscopes, two-photon microscopes, and STED super-resolution.

Biomedical Photonic Technologies, First Edition. Edited by Zhenxi Zhang, Shudong Jiang, and Buhong Li.

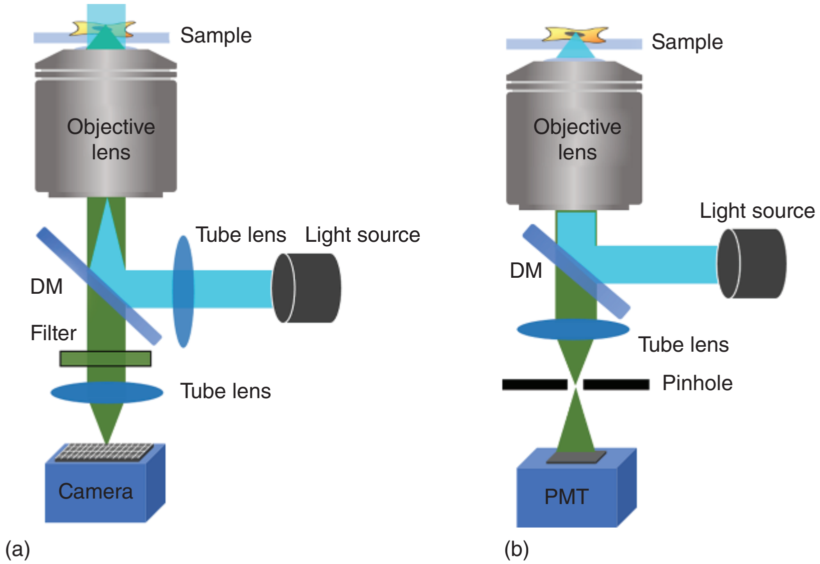

Figure 1.1 (a) Comparison of wide-field microscopy. (b) Point-scanning microscopy. Source: Chong Chen.

This chapter mainly introduces the advance of the wide-field fluorescent microscope in the last ten years. We first introduce the methods to improve the optical sectioning and the resolution by structured illumination, then introduce the methods by light sheet illumination. The optical principle, setup, image processing method will be introduced in each section. The chapter ends with a prospect for future development.

1.2 Optical Sectioning by Structured Illumination

1.2.1 Optical Section in Wide-Field Microscopy

The optical section in microscopy defines its capability to resolve structure axially. In an epi-fluorescent microscope, the entire sample space is illuminated, and all of the excited fluorescence signals collected by the objective can go into the array detector. Consequently, when the sample goes out of focus, its image becomes blurred, but the signals do not disappear. This problem presents a significant hindrance in wide-field microscopy.

In optical microscopy, the depth of focus is how far the sample plane can move while the specimen remains in perfect focus. The numerical aperture of the objective lens is the main factor that determines the depth of focus (D):

$$D = (\lambda \cdot n)/NA^2 + (D_n/(M \cdot NA)) \cdot e \tag{1.1}$$

where λ is the wavelength of the fluorescent light, n is the refractive index of the medium [usually air (1.000) or immersion oil (1.515)], NA is the numerical aperture

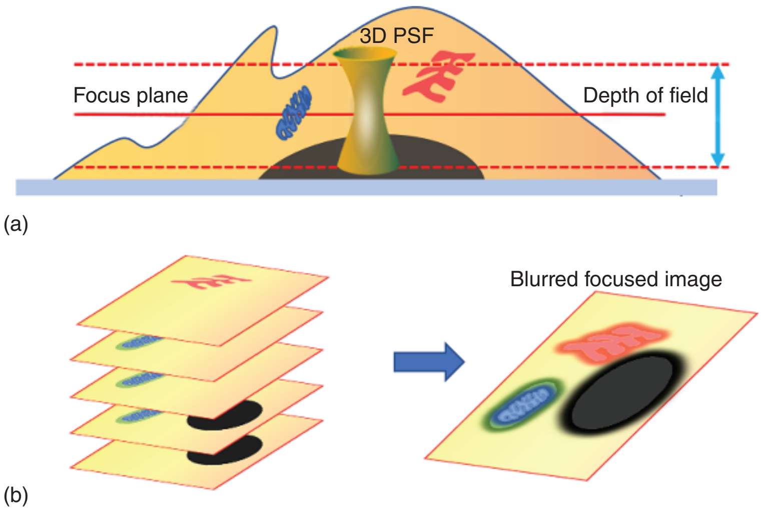

Figure 1.2 (a) Sketch of the depth of field. (b) The defocused signals cause blur of the focused image. Source: Chong Chen.

of the objective lens. The variable e is the smallest distance that can be resolved by a detector that is placed in the image plane of the microscope objective, whose lateral magnification is *M*. For a high-end fluorescent microscope with *NA* 1.4 and a 100× magnification objective, the depth of focus is on the order of 500 to 700 nm, dependent on the fluorescent wavelength. This depth of field defines the best optical section capability for an epi-fluorescence microscope.

However, when imaging samples with a thickness larger than the microscope's depth-of-focus, the sample's out of focus plane is also excited and forms a defocus image at the camera plane (Figure 1.2). The superimposition of these defocus images lowers the contrast of the camera's captured image and practically lowers the axial resolution. The imperfections in the microscope's optics and the scattering of fluorescence signals by the sample itself make the situation even worse. So, the priority demand to improve the wide-field microscope's performance lies in eliminating the out-of-focus signal, yielding better optical sectioning capability.

1.2.2 Principle of Optical Section with Structured Illumination

In a laser scanning confocal microscope, the out-of-focus light is rejected using a pinhole. In a wide-field microscope, no pinhole can be used since it uses a array detector. One way to reject the out-of-focus signals is by using structured illumination. By utilizing a grating or a digital mirror device (DMD), stripe patterns were projected on the image plane so that a structured illumination was created to excite the fluorescence molecules within the focus plane. The actual focus range of the stripes can be made very sharp if the proper period of the grating is used. Out of focus, the strip patterns become uniform, which will generate a nonmodulated background. Therefore, the image formed by the microscope will consist of striped in-focus features superposed with uniformly illuminated out-of-focus features. A postprocessing algorithm could reject this background afterward, thus obtaining a better optical section capability.

So, to obtain optical sectioning with structured illumination, two factors are needed: optical instrumentation to create structured illumination and the optical section reconstruction algorithm. These two aspects will be discussed in the following section.

1.2.3 Methods for Generating Create Structured Illumination

For structured illumination, the excitation light field needs to be patterned, and the pattern needs to be shifted or rotated to capture all sample information. Several methods have been developed for this purpose.

(1) The fluorescence grating imager inserts a grid into the field diaphragm plane of a fluorescence microscope (Figure 1.3). The shift of the grid projection can be achieved by translating the grate or tilting a plane-parallel glass plate located directly behind the grid. This method requires very little modification to the microscope, so it is easy to implement and low cost. Zeiss, Inc. uses the technique in their APOTOME equipment for 3D imaging [1]. However, the image speed is limited by the mechanical movement of the grate or the glass plate. Generally, 10 frames per second could be obtained, which is not fast enough for some subcellular dynamics imaging. Another drawback is that the period of a grate is fixed, so one has to change the grid if one wants to use a different period.

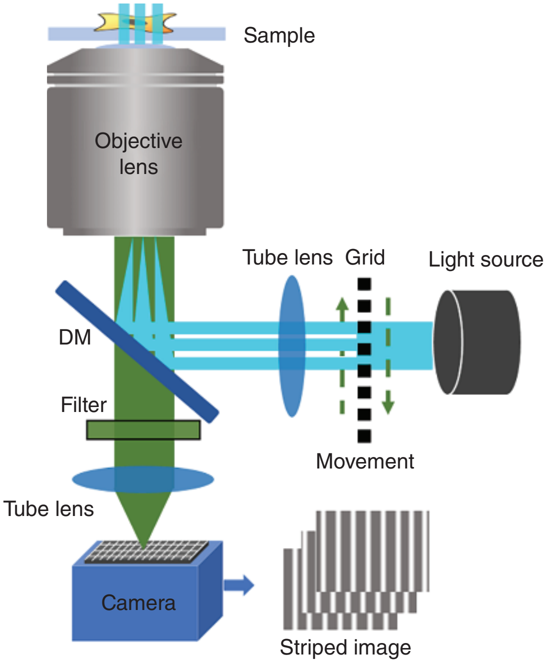

Figure 1.3 Structured illumination with grating for optical section. Source: Chong Chen.

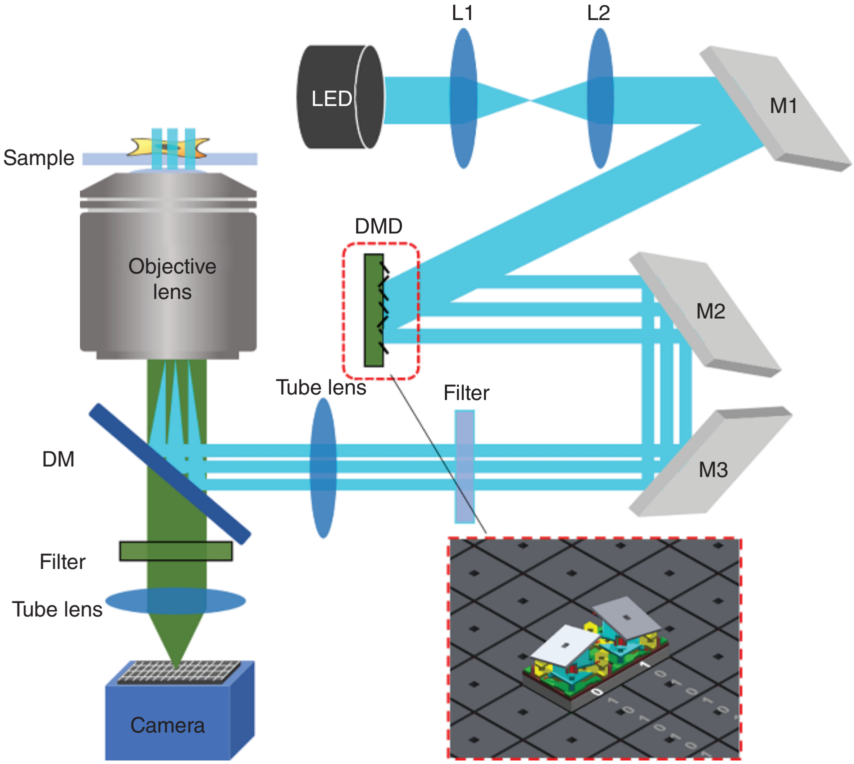

Figure 1.4 Structured illumination with digital mirror device. Source: Chong Chen.

(2) To avoid mechanical translation, a DMD was introduced to project fringe patterns on the sample plane [2]. The DMD is a micro-electro-mechanical system (MEMS) consisting of a few hundred thousand tiny switchable mirrors with two stable mirror states (such as, −12° and +12°). When a micromirror is set at +12° toward the illumination, it is referred to as an "on" state. Similarly, at the position of −12° it is referred to as the "off" state. The mirrors are highly reflective and have a higher refreshing speed and a broader spectral response (Figure 1.4). However, since DMD is a reflective device and has to be positioned at 12° in the light path, the optical layout using DMD is more complex than using grate [3–6].

(3) Structured illumination could also be realized using an LED array as a light source, as implemented by V. Poher et al. [7]. The microstructured light source is an InGaN LED consisting of 120 side-by-side and individually addressable microstripe elements. Each stripe of the device is 17 microns wide and 3600 microns long, with a center-to-center spacing between stripes of 34 microns, giving an overall diode structure size of 3.6 × 4.08 mm. A dedicated electrical driver was constructed to allow arbitrary combinations of the stripes to be driven simultaneously to produce programmable line patterns (Figure 1.5). Using LED

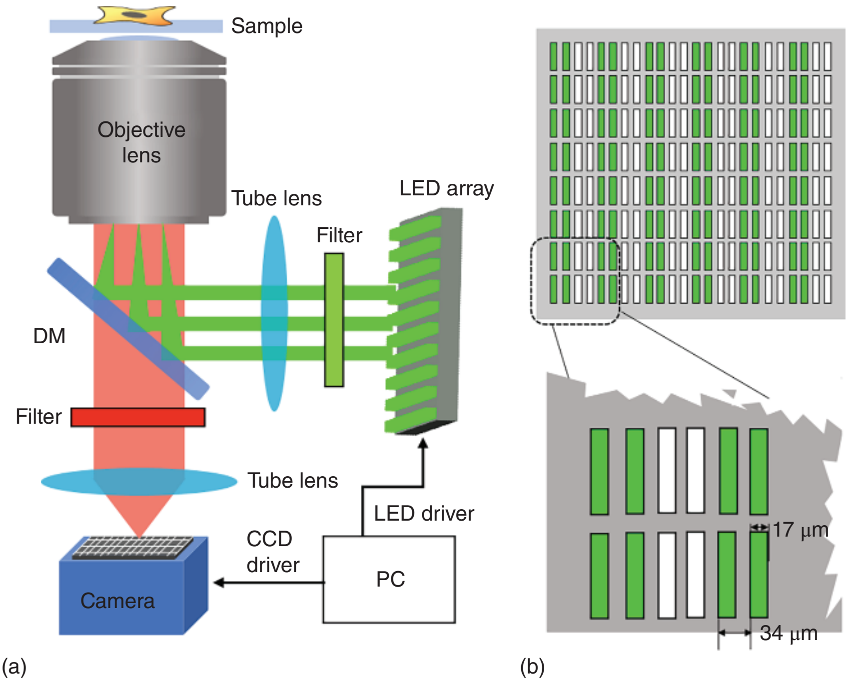

Figure 1.5 Structured illumination with LED array. (a) Schematic of structured illumination microscopy; (b) Schematic of LED array. Source: Chong Chen.

array for structured illumination does not require modification of the microscope setup, only a change of the light source. The whole system contains no moving parts, and the LED array could display up to 50 000 independent line patterns per second. However, the brightness of the array LED is still limited at this point.

(4) Instead of a well-defined strip pattern, structured illumination could also be random speckle patterns from a laser, as invented by J. Mertz group [8]. Speckle patterns are random and granular-intensity patterns that exhibit inherently high contrast. Fluorescence images obtained with speckle illumination are therefore also granular; however, the contrast of the observed granularity provides a measure of how in focus the sample is: High observed contrast indicates that the sample is dominantly in focus, whereas low observed contrast indicates it is dominantly out of focus. The diffuser randomizes the phase front of the laser beam, resulting in a speckle pattern that is projected into the sample via a microscope objective. To obtain the latter, random the speckle patterns are applied within a single exposure of the camera, effectively simulating uniform illumination. Randomization of the speckle pattern is easily achieved by translating or rotating the diffuser (Figure 1.6). When the diffuser is static, the speckle illumination exhibits high contrast (top right panel). When the diffuser is rapidly

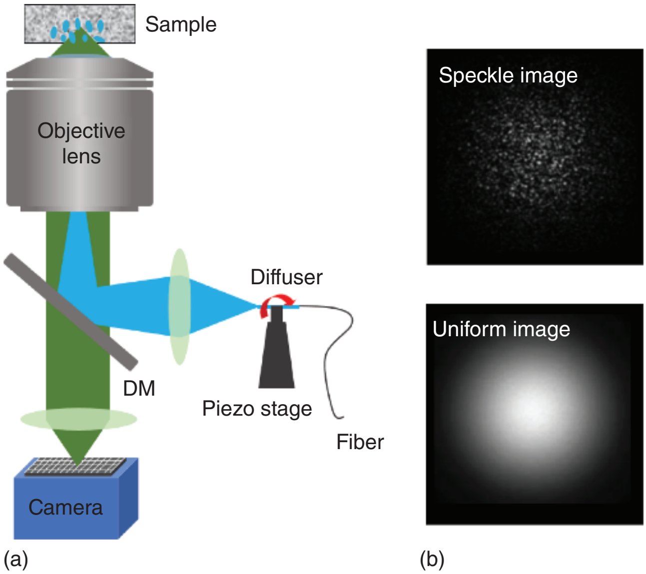

Figure 1.6 Structured illumination with random speckle patterns. (a) Schematic of speckle illumination microscopy; (b) random speckle illumination image and uniform wide-field image. Source: Chong Chen.

oscillated by a galvanometric motor, the resulting speckle becomes blurred over the course of the camera exposure, effectively simulating uniform illumination (bottom right panel). The observed speckle contrast thus serves as a weighting function, indicating the in-focus to out-of-focus ratio in a fluorescence image. While effective, this technique proved to be slow since several images were required to obtain an accurate estimate of speckle contrast A later implementation involved evaluating speckle contrast in space rather than time, using a single image [9].

1.2.4 Optical Section Algorithms with Structured Illumination

In optical section imaging with structured illumination, multiple images were captured for each layer with the same strip period but different phases. An afterwards reconstruction algorithm is then used to calculate a sectioned image from the multiple raw data points. By now, several different algorithms have been developed with different performance.

1.2.4.1 Simple Reconstruction Algorithm

The optical system consists simply of an illumination mask $S(t_0, w_0)$, which is imaged onto an object of amplitude transmittance or reflectance $\tau(t_1, w_1)$ the final image is recorded by a CCD camera in the image plane (t, w) [10, 11]. The mask is illuminated incoherently, which permits us to write the image intensity as

$$I(t,\omega) = \iint S(t_0, w_0) \left| \iint h_1\left(t_0 + t_1, w_0 + w_1\right) \times \tau\left(t_1, w_1\right) h_2\left(t_1 + t, w_1 + w\right) dt_1 dw_1 \right|^2 dt_0 dw_0 \tag{1.2}$$

where $h_{1,2}$ represents the amplitude point-spread function (PSF) of the optical system. The optical coordinates $(t,\ w)$ that are related to real coordinates $(x,\ y)$ through $(t,\ w) = (2\pi/\lambda)(x,\ y)n \cdot \sin\alpha$ where $n \cdot \sin\alpha$ is the numerical aperture (NA) and λ denotes the wavelength.

The illumination mask takes the form of a one-dimensional grid and can be written for simplicity as

$$S(t_0, w_0) = 1 + m \cdot \cos(\widetilde{v} t_0 + \phi_0) \tag{1.3}$$

where m denotes a modulation depth and ϕ_0 is an arbitrary spatial phase. The normalized spatial frequency $\widetilde{v}$ is related to the actual spatial frequency v through $\tilde{v} = \beta \cdot \lambda \cdot v/NA$, where β denotes the magnification between the grid plane and the specimen plane. And then, Eq. (1.3) was substituted into Eq. (1.2),

$$I(t, w) = I_0 + I_c \cos\phi_0 + I_s \sin\phi_0 \tag{1.4}$$

where I_0 represents a conventional wide-field image. I_c and I_s represent the images that are due to masks of forms $m \cdot \cos(\widetilde{v} t_0)$ and $m \cdot \sin(\widetilde{v} t_0)$, respectively. These definitions suggest that if we are able to form $I_p = \left(I_c^{\ 2} + I_s^{\ 2}\right)^{1/2}$. We would remove the grid pattern from the image of the specimen. This result could be readily achieved by taking three images, I_1, I_2, and I_3, which correspond to the relative spatial phases 0, $\phi_0 = 2\pi/3$, and $\phi_0 = 4\pi/3$, respectively. So,

$$I_p = \left[(I_1 - I_2)^2 + (I_1 - I_3)^2 + (I_2 - I_3)^2\right]^{1/2} \tag{1.5}$$

which is analogous to square-law detection in communications systems. Alternatively, Ip can be formed as

$$I_p = \left| I_1 + I_2 \exp j\frac{2\pi}{3} + I_3 \exp\frac{4\pi}{3} \right| \tag{1.6}$$

which is the equivalent of homodyne detection. We note that the conventional image, I_0, can be recovered from $I_1 + I_2 + I_3$.

1.2.4.2 *HiLo* Reconstruction Algorithm

HiLo microscopy is based on the acquisition of two images with different type of illumination in order to obtain one optically sectioned image (Figure 1.7) [12, 13]. A uniform-illumination image is used to obtain the high-frequency (Hi) components of the image, and a nonuniform-illumination image is used to obtain the low-frequency (Lo) components of the image. The corresponding intensity distributions of the uniform- and structured-illumination images are denoted as $I_u(\vec{r})$ and

$I_n(\vec{r})$, respectively. The intensity distributions of the high- and low-frequency images are referred to as $I_{Hi}(\vec{r})$ and $I_{Lo}(\vec{r})$ with the spatial, two-dimensional coordinates $\vec{r}$. The resulting full-frequency optically sectioned image is then obtained by

$$I_{HiLo}(\vec{r}) = I_{Hi}(\vec{r}) + \eta I_{Lo}(\vec{r}) \tag{1.7}$$

with η being a scaling factor that depends on the experimental configuration of the setup.

In order to obtain the high-frequency in-focus components, a typical characteristic of the optical transfer function (OTF) of a standard wide-field microscope is exploited: high-frequency components are only well-resolved as long as they are in-focus, while low-frequency components remain visible even if they are out-of-focus. Hence, high-frequency components are directly extracted by $I_u(\vec{r})$ using

$$I_{Hi}(\vec{r}) = HP\{I_u(\vec{r})\} \tag{1.8}$$

whereby HP denotes a Gaussian high-pass filter with the cutoff frequency k_c applied in the frequency domain.

The low-frequency component of the image is obtained by calculating

$$I_{Lo}(\vec{r}) = LP\{C_S(\vec{r})I_u(\vec{r})\} \tag{1.9}$$

with the complimentary low-pass filter LP. The speckle contrast $C_S(\vec{r})$ acts as a weighting function for extracting the in-focus contributions and rejecting the out-of-focus contributions of the uniform-illumination image $I_u(\vec{r})$. The overall spatial contrast $C_n(\vec{r})$ is influenced by the speckles in the illumination as well as sample-induced speckles. In order to correct for the influence of the sample-induced speckles, the difference image

$$I_\delta(\vec{r}) = I_n(\vec{r}) - I_u(\vec{r}) \tag{1.10}$$

is used for speckle contrast calculation. The speckle contrast is defined as

$$C_S(\vec{r}) = \frac{\langle \sigma_\delta(\vec{r}) \rangle_A}{\langle I_n(\vec{r}) \rangle_A} \tag{1.11}$$

where $\langle I_n(\vec{r}) \rangle_A$ and $\langle \sigma_\delta(\vec{r}) \rangle_A$ are the mean of $I_n(\vec{r})$ and the standard deviation of I_δ, respectively. The speckle contrast is calculated over a partition of local evaluation areas A. It is assumed that each area is large enough to encompass several imaged speckle grains. The axial resolution is further increased by applying the band-pass filter

$$W(\vec{k}) = \exp\left(-\frac{|k^2|}{2\sigma_w^2}\right) - \exp\left(-\frac{|k^2|}{\sigma_w^2}\right) \tag{1.12}$$

to the difference image I_δ before evaluating $\langle \sigma_\delta(\vec{r}) \rangle_A$. As a result, the optical sectioning depth of the Lo-component can be adjusted by tuning σ_w. In order to also adjust the optical sectioning depth of the Hi-component, the cutoff frequency of the Gaussian high-pass filter is also tuned by setting $k_c = 0.18\sigma_w$. Since the high- and low-frequency components of the image are now determined, the resulting optically sectioned HiLo image is eventually obtained using Eq. (1.7). As a result, because

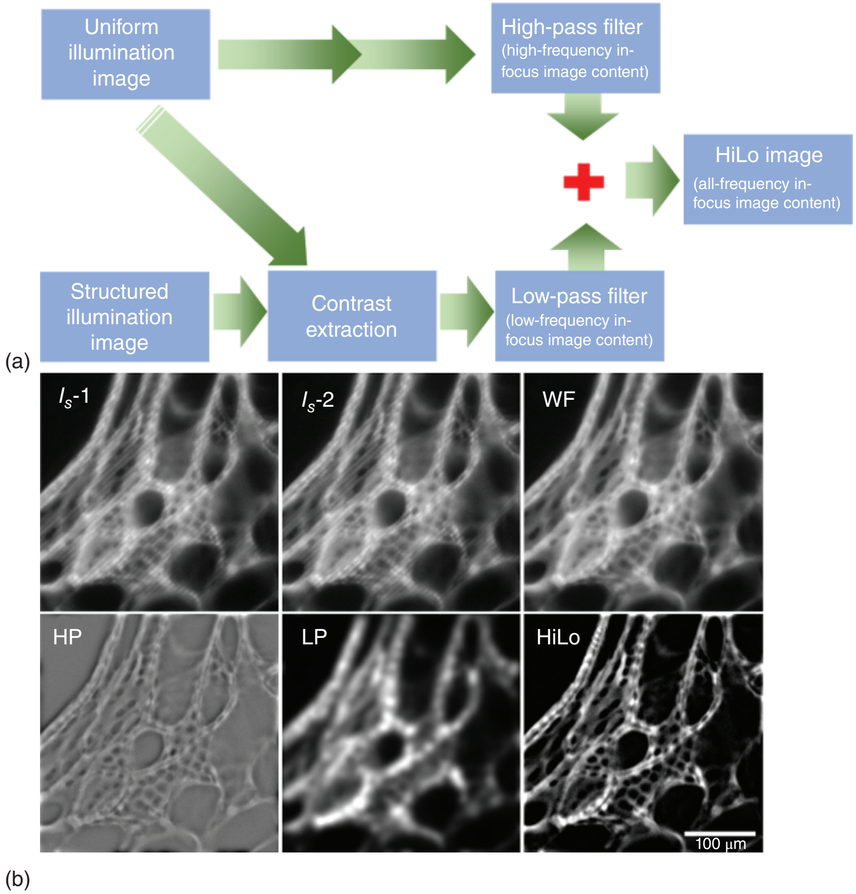

Figure 1.7 Algorithm for HiLo reconstruction. (a) The flow chart of HiLo algorithm; (b) A reconstruction of pumpkin stem section. I_s-1, I_s-2 structured illumination images; WF wide field image; HP high-pass filter image; LP low-pass filter image. Source: Chong Chen.

the measurements rates equals half of the camera framerate, the HiLo technique provides a powerful method for fast two-dimensional image acquisition.

1.2.4.3 Hilber–Huang Transform Reconstruction Algorithm

Xing zhou et al. propose a one-dimensional (1-D) sequence Hilbert transform (SHT) algorithm to decode the in-focus information (Figure 1.8) [14].

A key step of structured illumination microscopy (SIM) is to project a sinusoidal fringe onto the specimen of interest. Then, the captured structured images can be decomposed into the in-focus and the out-of-focus components:

$$I_{cap}(x,y) = I_n(x,y) + I_m(x,y) \cdot \sin(2\pi \nu x + \varphi) \tag{1.13}$$

where I_n is the out-of-focus background, I_m is the in-focus information, ν and φ are the spatial frequency and initial phase of the projected sinusoidal fringe, respectively. Because the intensity of the out-of-focus background I_n remains constant, we can subtract two phase-shifting raw images to eliminate the background. Thus, we obtain an input image I_s with sinusoidal amplitude modulation described in Eq. (1.14):

$$I_s(x,y) = I_m(x,y) \cdot \cos(2\pi \nu x + \varphi_s) \tag{1.14}$$

where φ_s is the mean value of the two arbitrary initial phases of the two raw images. The next step is to demodulate the sinusoidal amplitude and obtain the in-focus information I_m from Eq. (1.14). It is seen that Im can be solved out by Eq. (1.14) directly. However, as a result of this, I_m becomes extremely sensitive to the precision of φ_s. Thus, I_s must be decoded by other ways to eliminate the residue sinusoidal pattern. Here, we utilize the Hilbert transform (HT) and construct a complex analytical signal I_A that is presented in the form of:

$$I_A(x,y) = I_s(x,y) + i \cdot I_{SH}(x,y) \tag{1.15}$$

where i is the imaginary unit and the imaginary part I_{SH} of I_A is the HT of the input pattern I_S. In optical interferometry, the interferograms may contain complex structures, including different frequency components. Therefore, the decoding process must be based on the 2-D HT. However, in SIM, the projection fringe contains only a single spatial frequency in one orientation (either x direction or y direction). So, the 2-D image I_S can be simplified as the combination of a sequence of 1-D sinusoidal amplitude modulation signals. In this case, the 1-D signal processing algorithm can be used for the 2-D image demodulation. In 1-D signal analysis, the HT is a powerful tool to achieve demodulation signal. Based on the characteristics of the HT, the HT of a cosine-modulated function becomes a sine-modulated function:

$$\begin{aligned} HT_x\{b(x) \cdot \cos x\} &= {}^1\!/\!_2[HT_x\{b(x) \cdot e^{ix}\} + HT_x\{b(x) \cdot e^{-ix}\}] \\ &= {}^1\!/\!_2[-i \cdot b(x) \cdot e^{ix} + b(x) \cdot e^{-ix}] \\ &= b(x) \cdot \sin x \end{aligned} \tag{1.16}$$

where HT_x denotes the HT operation in x direction. Applying the 1-D Hilbert transform to the I_s, we obtain the analytical signal:

$$\begin{aligned} I_A(x,y) &= I_S(x,y) + i \cdot HT_x\{I_S(x,y)\} \\ &= I_m(x,y)\cos(2\nu x + \varphi_s) + i \cdot I_m(x,y)\sin(2\nu x + \varphi_s) \end{aligned} \tag{1.17}$$

Finally, the optically sectioned image I_m can be obtained by

$$I_m(x,y) = |I_A(x,y)| \tag{1.18}$$

1.3 Super-Resolution Imaging with Structured Illumination

1.3.1 Lateral Resolution in a Wide-Field Microscope

Lateral resolution gets more attention in optical microscopy since it directly determines the finest structures that can be resolved. The lateral resolution of the optical system and the pixel size of the camera are the two factors that need to be

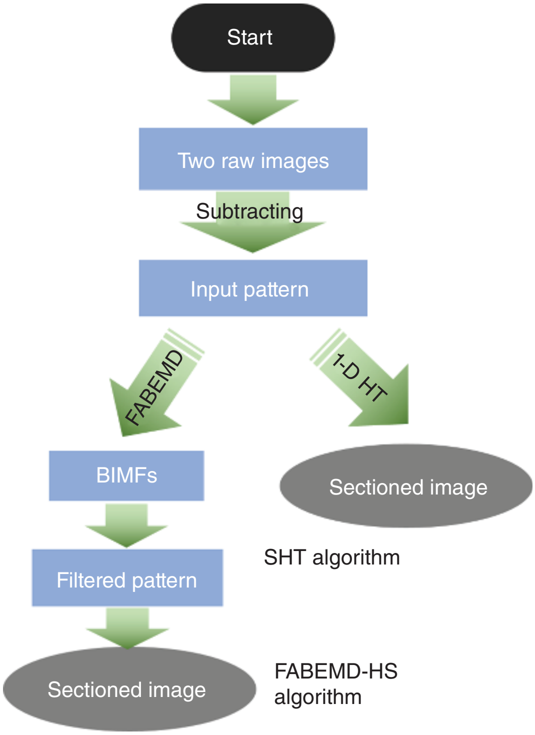

Figure 1.8 Optical section algorithms with Hilber–Huang transform. Source: Chong Chen.

considered first for magnification of the optical system. According to the Nyquist sampling rule, the pixel resolution (pixel size divided by the magnification) should be at least half of the feature size to be observed.

However, in optical microscopy, the lateral resolution is determined not only by the pixel resolution but also by the PSF. Due to the wave diffraction of light, a collimated light focused by the optical system won't be an infinite point but a diffraction-limited optical spot. Similarly, a point-like object will be imaged by an optical system as a blurry spot with a finite size. The intensity distribution of the spot is defined as the PSF. The lateral PSF in 2-D can be described as an airy pattern or approximated as a Gaussian function in general. The PSF depends on the light wavelength and numerical aperture of the imaging objective (Figure 1.9).

Two point-like objects next to each other will be imaged as the superposition of two corresponding PSFs. When the two point-like objects are too close to each other, they cannot be resolved as separate points. The lateral resolution of an optical system can be defined as the minimum resolvable distance between two point-like objects in the image, as Rayleigh criteria:

$$d_{\min} = 0.61\frac{\lambda}{NA} \tag{1.19}$$

Another way to define the resolution is by utilizing the OTF. The OTF is the Fourier transform of the PSF. The resolution of a light microscope is determined by

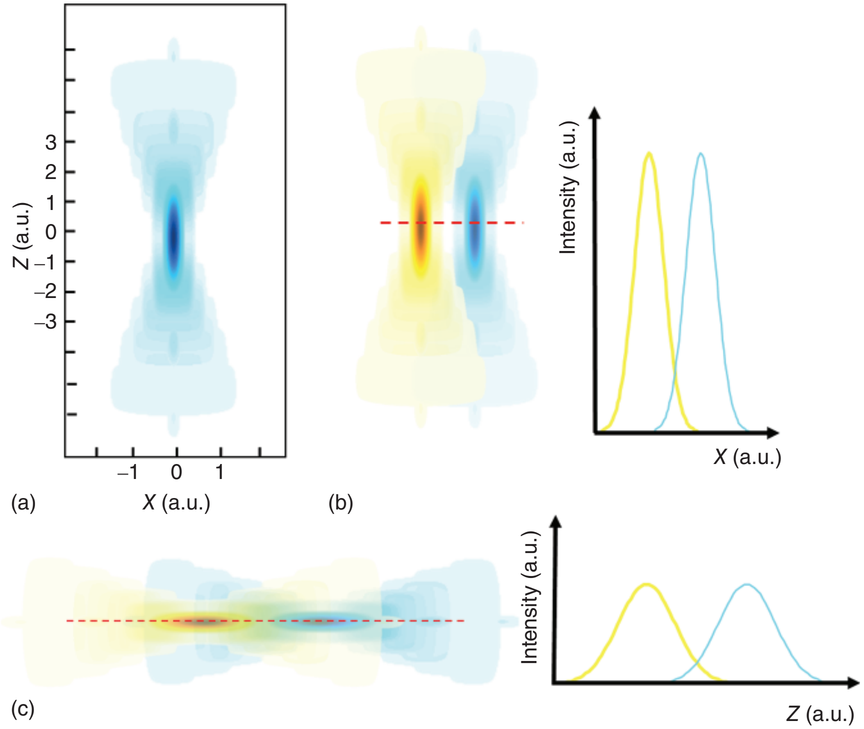

Figure 1.9 (a) Vertical sections through the 3D PSFs and resulting definition. The contrast has been greatly enhanced to show the weak side lobes (which are the rings of the airy disk, viewed edge on). (b) Schematic of horizontal resolution definition. (c) Schematic diagram of axial resolution definition. Source: Chong Chen.

the cutoff frequency of the OTF:

$$f_{cut-off} = \frac{1}{d_{\min}} = 2\frac{NA}{\lambda} \tag{1.20}$$

Only those spatial frequencies coming from the object that is inside the support of the OTF, i.e. smaller than the cut-off frequency, are detectable. In the last twenty years, several super-resolution techniques have been developed to break the diffraction limit and have been widely used in many biological applications. In the following, the structured illumination microscopy technique is introduced as a typical wide-field super solution microscope that is mostly suitable for live cell dynamic imaging.

1.3.2 Principle of Super-Resolution SIM

In 2000, Gustafsson, M. G., proposed a wide-field imaging technique with resolution beyond the diffraction limit by structured illumination [15]. The principle is to project a spatially patterned illumination onto the sample such that Moiré fringes are created. The recorded Moiré fringes of the fluorescent image contain the frequency of both the illumination structure and the spatial frequencies of the sample.

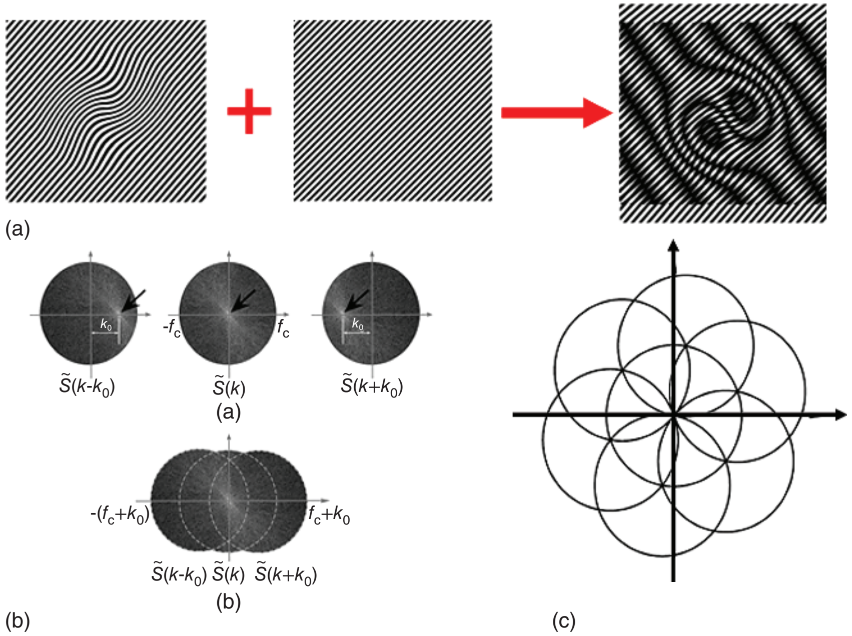

Figure 1.10 Principle of the super-resolution SIM. (a) Schematic of structured illumination pattern; (b) 2D OTF of SIM with excitation pattern in only one orientation. (c) 2D OTF of SIM with excitation pattern in three orientation. Source: Chong Chen.

High spatial frequency information of the sample, which was outside the passband of the microscope's OTF is now downmodulated into the passband of the OTF. By acquiring several images, a super-resolved SIM image can be reconstructed through computational reconstruction (Figure 1.10). In order to achieve isotropic resolution improvement, nine images of three orientation angles with three phases of each orientation angle are usually acquired. In the last twenty years, the SR-SIM technique has been greatly studied and improved, which has now become the most popular super-resolution technique for live cell dynamic imaging. With linear excitation, linear SIM could achieve a twofold resolution improvement [16]. Nonlinear SIM had no theoretical resolution limit and experimentally attained better than 40 nm resolution with saturated excitation [17] or sequential activation & excitation [18].

Despite the fact that structured illumination was used in both optical sectioning and super-resolution, the principle, optical setup, and image reconstruction algorithms are quite different. The structure illumination in OS-SIM is generally formed by the projection of a fringe pattern onto the microscope field of view (FOV) using a noncoherent light source, while the structure illumination for SR-SIM is typically formed by laser interference because of the thinner pattern period required.

1.3.3 SR-SIM Setup Based Laser Interference

Many early SIM systems that use a mechanically moving physical grating to generate the spatial patterned illumination cannot guarantee the precise shift of the

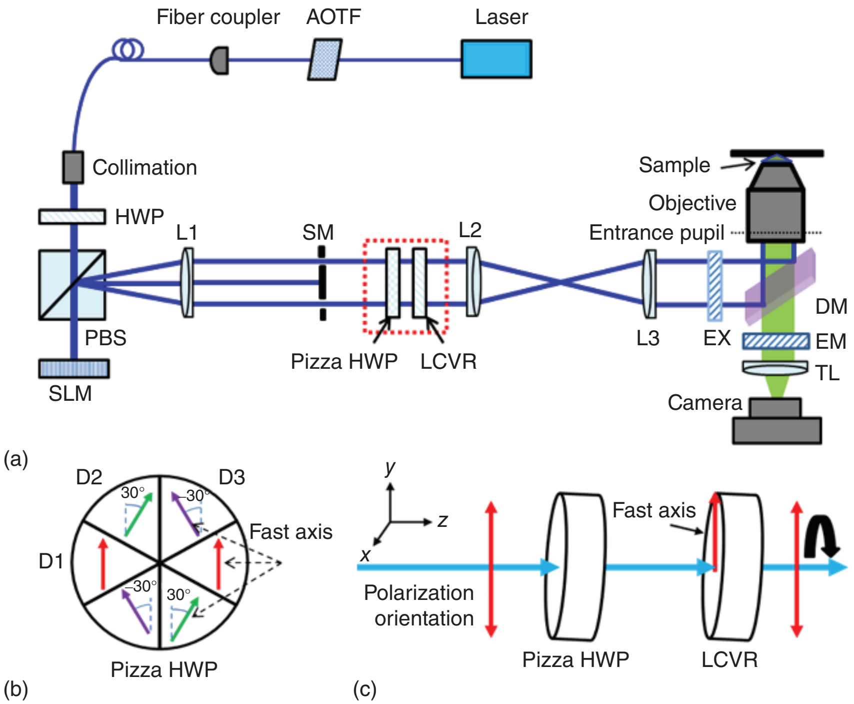

Figure 1.11 The layout of the 2D-SIM setup based on the proposed polarization optimization method. (a) Schematic of interference structured illumination microscopy; (b) Polarization of three orientation; (c) Schematic of polarization control method. Source: Chong Chen.

illumination pattern during image acquisition [16, 19]. The spatial light modulator (SLM)-based SIM system arose from the need for fast illumination pattern switching and an accurate pattern shift for video-rate observation in living cells [20, 21].

A ferroelectric-liquid-crystal-on-silicon (LCoS) display used as a SLM has two stable crystal axes driven by an applied voltage. Due to the pixelated structure of the display, additional unwanted diffraction orders are created and lead to a jagged edge in the illumination pattern in the sample plane. In SIM, a Fourier filter is used to block those unwanted diffraction orders. In the two-beam SIM system, the zeroth illumination order is blocked (Figure 1.11). Only the ±1st diffraction orders pass through the objective and form an interference pattern in the sample plane. This leads to the same interference pattern in the sample plane for both the grating pattern and its inverse image displayed on the SLM.

Fast switching up to several kHz is offered by ferroelectric SLMs. However, low diffraction efficiency is a major drawback. In addition, the SLM has to display the inverse image of the previous grating pattern to prevent damage to the LCoS. Nevertheless, as the required illumination intensity for acquiring raw SIM images is relatively low, it is preferable to use a ferroelectric SLM to modulate the illumination light.

The simplified sketch of the first prototype of the fastSIM setup is shown in Figure 1.11. An acousto-optical tunable filter (AOTF) right behind the CW laser ensures precise and fast switching of the illumination light. An illumination grating pattern is generated by an SLM placed in the intermediate image plane and is projected on the sample. In order to achieve high contrast of the illumination grating in the sample plane, a liquid crystal variable retarder (LCVR) and a customized azimuthally patterned polarizer (pizza polarizer) are placed after the SLM to achieve azimuthal polarization. A passive mask as a Fourier filter is used to block all unwanted diffraction orders except the ±1st diffraction orders.

Polarization modulation is the most important part of the SIM optical path. In addition to the above methods, more optimized schemes have been developed in recent years. A polarization beam splitter (PBS) in this scheme was used to shorten the length of the optic path. In order to modulate the polarization of ±1 order diffraction beams in three different orientations, a combinatorial waveplate composed of six fan-shaped achromatic Pizza HWPs was employed. Three orientations corresponding to illumination light are defined as D1, D2, and D3, respectively. The fast axes of the two opposite HWPs for D1 are set to be parallel to the electrical vibration direction of the incident beam. The fast axes of the remaining four HWPs of D2 and D3 are rotated by +30° and −30°, respectively. The polarization of the ±1-order diffraction beams is rotated by 0° and ±60° in three orientations, corresponding to the above fast-axis rotation. After pizza HWP modulation, an LCVR is utilized to compensate for the additional phase generated by the dichroic mirror (DM). The fast axis of the LCVR is set to be parallel to the electrical vibration direction of the incident beam, as shown in Figure 1.11.

1.3.4 Super-Resolution Reconstruction for SIM

Linear super-resolution structured illumination microscopy (SR-SIM) is a wide-field imaging method that doubles the spatial resolution of fluorescent images [22]. The final SR image is reconstructed by postprocessing image algorithms. Here, we first briefly introduce the principle and implementation of the conventional Wiener SIM reconstruction algorithm (hereinafter referred to as "Wiener-SIM"). We start by considering a two-dimensional (2D) SIM raw data of the form

$$\begin{aligned} D_{\theta,n}(r) \cong {} & \{S_{in}(r) \cdot [1 + m_\theta \cos(2\pi k_\theta \cdot r + \varphi_\theta + 2\pi \cdot (n-1)/3)]\} \otimes PSF(r) \\ & + S_{out}(r) + N(r) \end{aligned} \tag{1.21}$$

where subscript θ and n are the orientation and phase of the illumination pattern ($\theta = 1,2,3$, $n = 1, 2, 3$); r is the image spatial coordinates; $S_{in}(r)$ is the sample on the objective focal plane; m_θ, k_θ, and φ_θ are the modulation, spatial frequency and initial phase of the illumination pattern in the raw data, respectively; symbol $\otimes$ denotes the convolution operation; $PSF(r)$ is the PSF of the microscope, $S_{out}(r)$ is out-of-focus background fluorescent signal, and $N(r)$ is noise.

The spectrum of SIM raw data can be obtained in the frequency domain by implementing Fourier transform to Eq. (1.21)

$$\tilde{D}_{\theta,n}(k) \cong \left[\frac{m_\theta}{2}\cdot\overline{S}_{in}(k+k_\theta)\cdot e^{-j\left(\varphi_0+{2\pi(n-1)}/{3}\right)}+\overline{S}_{in}(k)+\frac{m_\theta}{2}\cdot\overline{S}_{in}(k-k_\theta)\cdot e^{j\left(\varphi_0+{2\pi(n-1)}/{3}\right)}\right] \cdot\overline{H}(k)+\overline{S}_{out}(k)+\overline{N}(k) \tag{1.22}$$

where $\overline{H}(k)$ is the OTF of the microscope, which is the Fourier transform of $PSF(r)$. $\overline{S}_{in}(k)$ is the spectrum components of the sample at the focal plane, $\overline{S}_{in}(k \pm k_\theta)$ are the spectrum components that contain the unresolvable high-frequency signals. $\overline{S}_{out}(k)$ and $\overline{N}(k)$ are the spectrum of the out-of-focus background and noise signal, respectively.

For 2D-SIM, the raw data of three different phases are collected in the same orientation, and all the spectrum components in Eq. (1.22) can be separated by solving Eq. (1.23)

$$\begin{bmatrix}\overline{S}_{\theta,0}(k)\\ \overline{S}_{\theta,+1}(k+k_\theta)\\ \overline{S}_{\theta,-1}(k-k_\theta)\end{bmatrix}=\begin{bmatrix}1 & e^{-j\varphi_0} & e^{j\varphi_\theta}\\ 1 & e^{-j\left(\varphi_\theta+{2\pi}/{3}\right)} & e^{j\left(\varphi_\theta+{2\pi}/{3}\right)}\\ 1 & e^{-j\left(\varphi_\theta+{4\pi}/{3}\right)} & e^{j\left(\varphi_\theta+{2\pi}/{3}\right)}\end{bmatrix}^{-1}\cdot\begin{bmatrix}\tilde{D}_{\theta,1}(k)\\ \tilde{D}_{\theta,2}(k)\\ \tilde{D}_{\theta,3}(k)\end{bmatrix} \tag{1.23}$$

To accurately extract the separated components in Eq. (1.23), and then shift them to the correct position, the correct illumination pattern parameters of m_θ, k_θ, and φ_θ should be accurately determined from the raw data. Typically, these reconstruction parameters can be estimated by cross-correlation methods. In this chapter, we developed a robust reconstruction parameter by combining normalized cross-correlation and spectrum notch for determining the correct reconstruction parameters.

Then, these separated components are shifted back to their correct position with sub-pixel precision

$$\begin{cases}\overline{C}_{\theta,0}(k)\cong\overline{S}'_{\theta,0}(k)\\ \overline{C}_{\theta,+1}(k+k_\theta)\cong FFT\left\{e^{j\left(\varphi_\theta+{2\pi}/{3}\right)}\cdot FFT^{-1}\left[\overline{S}'_{\theta,+1}(k+k_\theta)\right](r)\right\}(k)\\ \overline{C}_{\theta,-1}(k-k_\theta)\cong FFT\left\{e^{-j\left(\varphi_\theta+{4\pi}/{3}\right)}\cdot FFT^{-1}\left[\overline{S}'_{\theta,-1}(k+k_\theta)\right](r)\right\}(k)\end{cases} \tag{1.24}$$

where $\overline{C}_{\theta,0}(k)$, $\overline{C}_{\theta,+1}(k+k_\theta)$, and $\overline{C}_{\theta,-1}(k-k_\theta)$ are the shifted spectrum components.

Thus, the reconstructed spectrum of SR-SIM can be obtained by the traditional generalized Wiener filtering deconvolution

$$\overline{S}_{SR}(k)=\frac{\sum_{\theta,L}\overline{C}_{\theta,L}(k+L\cdot k_\theta)\cdot H^*_{\theta,L}(k+L\cdot k_\theta)}{\sum_{\theta,L}|H_{\theta,L}(k+L\cdot k_\theta)|^2+W^2}\cdot\widetilde{A}(k) \tag{1.25}$$

where symbol * is the conjugate operation. w is the Wiener constant, which is an empirical value $\widetilde{A}(k)$ is the apodisation function used to suppress artifacts. In the Wiener-SIM we implemented, a theoretical OTF based on imaging conditions was employed as the apodization function

$$\widetilde{A}(k)=\frac{2b(|k|)-\sin[2b(|k|)]}{\pi} \tag{1.26}$$

Finally, the reconstructed SR image is

$$\overline{S}_{sr}(r) = FFT^{-1}\{\overline{S}_{initial-SR}(k) \cdot \widetilde{W}(k)\} \tag{1.27}$$

where symbol FFT^{-1} represents inverse Fourier transform.

Conventionally, the raw SIM data with high modulation contrast and high signal-to-noise ratio (SNR), the PSF that matches the imaging conditions during raw data acquisition, and the reconstruction algorithm with excellent artifact suppression performance are three key factors for obtaining SR-SIM images with minimum artifacts. In general, Wiener-SIM usually estimates the illumination pattern parameters from the raw SIM data and then reconstructs the SR images based on the generalized Wiener filtering deconvolution (Eq. (1.25)). However, Wiener-SIM is not the optimal solution for reconstructing high-quality SR-SIM images because it still faces the following challenges.

1.3.5 Typical Artifacts and Removement Methods

Typical artifacts often appear in SR-SIM images, such as "hatching," "honeycomb," "snowflake," "sidelobe," and "hammerstroke" artifacts, etc., resulting in the fidelity and quantification of SIM images always facing challenges [23]. To pursue high-quality SR images with minimal artifacts, many efforts have been made, including in-depth imaging system establishment protocol, accurate reconstruction parameter estimation, practical system calibration and sample preparation guidelines, the guide for user-defined parameters adjustment, and some open-source reconstruction tools. These works have prompted researchers to gain insight into the causes, features, and suppression methods of typical artifacts. So far, the sources of artifacts in SR-SIM images have been well studied and summarized in the recently published papers. Although many artifacts can be distinguished subjectively, they cannot be robustly eliminated, and certain artifacts still frequently appear in the SIM images of publications. The presence of artifacts limits the accessibility of SIM to a few experts, hindering its wider use as a general imaging tool. More importantly, new structures found using SIM must be interpreted with special care to avoid incorrectly identifying artifacts as real features [24–26].

To reduce reconstruction artifacts, Wiener-SIM usually emphasizes collecting raw data with high modulation contrast and a high SNR [27, 28]. However, in actual experiments, since the modulation contrast and SNR of the raw SIM data are mainly determined by the quality of illumination patterns, the contrast properties of the labeled biological samples, and the optical properties of the imaging system, the raw SIM data with high modulation contrast and high SNR cannot always be collected. For example, when implementing ultrafast SR-SIM imaging, it is easy to collect raw data with low SNR. Meanwhile, as the imaging depth increases, the modulation contrast of raw data will also gradually decrease due to the rapid enhancement of the out-of-focus background fluorescence. Moreover, when the contrast of the labeled sample is poor, even if the illumination pattern at the objective focal plane has high modulation contrast, the raw data shows low modulation contrast. Furthermore, raw data with suboptimal modulation contrast is also unavoidable in either home-built SIM systems or commercial SIM systems when imaging device states are imperfect and users are unskilled in operation.

For low SNR raw data, Wiener-SIM may not be able to estimate the correct pattern wave vectors, and noise-related artifacts in the reconstructed image are also more serious. For raw data with suboptimal modulation contrast, Wiener-SIM also faces the challenge that the correct reconstruction parameters may not be determined. For example, the estimated modulation depth is less than the actual value. According to Eq. (1.26), the smaller modulation factor can cause over-amplification of the high-frequency components, resulting in "snowflake" artifacts and artifacts related to high-frequency noise. In addition, for raw data with strong background fluorescence, out-of-focus fluorescence can cause "honeycomb" artifacts or "hammerstroke" artifacts.

In practice, in order to avoid the risk of artifacts, a large number of suboptimal raw data sets are not effectively utilized or even abandoned. This not only caused a waste of time and money in the SIM imaging experiment, but more importantly, limited the suitable application scenarios of SIM.

1.4 3D imaging with Light Sheet Illumination

1.4.1 Principle and History

Light sheet fluorescence microscopy (LSFM) uses a thin plane of light to optically section transparent tissues or whole organisms that have been labeled with a fluorophore. Compared with confocal and two-photon microscopy, LSFM is able to image thicker tissues (>1 cm) with reduced photobleaching and phototoxicity because the specimen is exposed only to a thin light sheet. In addition, LSFM is a nondestructive method that produces well-registered optical sections that are suitable for three-dimensional reconstruction and can be processed by other histological methods (e.g. mechanical sectioning) after imaging.

The first published account of a very simple version of an LSFM (called ultramicroscopy) was described by Siedentopf and Zsigmondy (1903), in which sunlight was projected through a slit aperture to observe gold particles. In 1993, Voie and colleagues developed a light sheet microscope system called orthogonal-plane fluorescence optical sectioning (OPFPS) [29]. OPFOS was developed by investigators in Francis Spelman's laboratory at the University of Washington who were attempting to quantitatively assess hair cell structure and other cochlear features to improve the cochlear implant. OPFOS featured all of the elements that are present in current LSFM devices—namely, laser, beam expander, cylindrical lens to generate the light sheet, specimen chamber, orthogonal illumination of the specimen, specimen movement for z-stack creation, and specimen clearing and staining for producing fluorescent optical sections. In 1994, an oblique illuminating confocal microscope was being developed in Ernst Stelzer's laboratory to improve the axial resolution

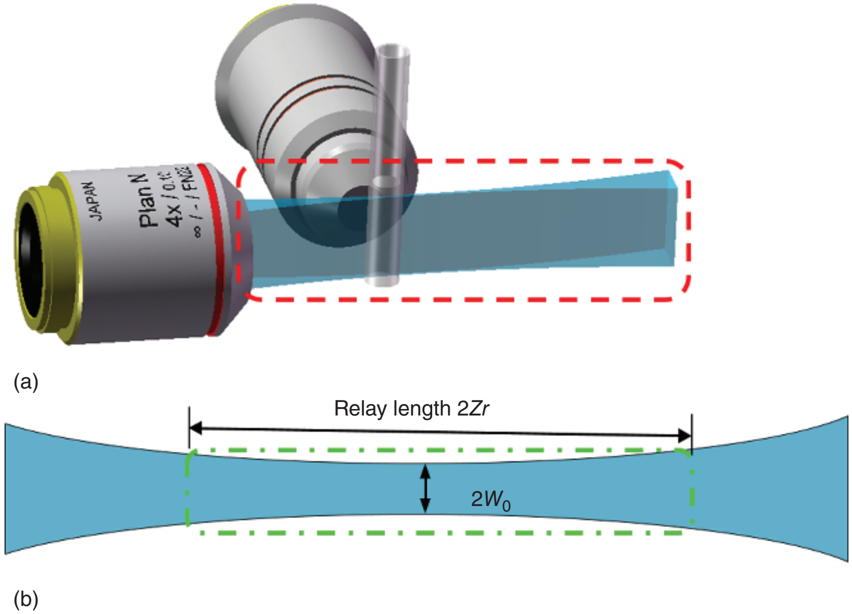

Figure 1.12 (a) Principle of light sheet. (b) The thickness and field of view of light sheet. Source: Chong Chen.

of confocal microscopy. It was called a confocal theta microscope [30, 31]. Theta confocal microscopy appeared to lay the foundation for their subsequent version of an LSFM device called selective or single-plane illumination microscopy (SPIM). As shown in Figure 1.12a, a typical light sheet microscope is an L-shaped structure composed of two objective lenses (one illumination objective and one detection objective).

Obviously, in a LSFM, the excitation and collection branches are uncoupled. Therefore, it is helpful to study both the excitation and collection arms of the LSFM separately. FOV lateral and axial resolution are the key parameters to be considered when constructing an LSFM system. In a LSFM, a focused light beam is used to produce the excitation LS (Figure 1.12). When using a Gaussian beam, its beam waist (w_0) can be related to the sectioning ability and, therefore, in a first approximation, to the axial resolution, R_{axial}, of the final image as

$$R_{axial} = 2w_0 = \frac{\lambda}{\pi\theta} = 2\frac{2\lambda f}{\pi D} = 2\frac{n\lambda}{\pi NA} \tag{1.28}$$

where f is focal length of the illumination objective, D is the entrance pupil diameter of illumination objective, and n is the refractive index. For a formal definition of resolution (see Section 1.2.1). Similarly, the Rayleigh range, Z_r, can be related to the FOV of the image and will be given by

$$FOV = 2Z_r = 2\frac{\pi w_0^2}{\lambda} \tag{1.29}$$

1.4.2 Light Sheet with Orthogonal Objectives

1.4.2.1 Light Sheet with Cylinder Lens

The Ernst H. K. Stelzer laboratory published the first true light sheet fluorescence microscopy article [32]. They used SPIM to visualize all muscles *in vivo* in the transgenic Medaka line Arnie, which expresses green fluorescent protein in muscle tissue. SPIM can also be applied to visualize the embryogenesis of the relatively opaque Drosophila melanogaster *in vivo*. The SPIM was capable of resolving the internal structures of the entire organism with high resolution (better than 6 μm) as deep as 500 μm inside the fish, a penetration depth that cannot be reached using confocal LSM. The L-type light sheet microscope's main components were shown.

A series of lasers provide lines for fluorescence excitation. An optical system that includes a cylindrical lens focuses the laser light onto a thin light sheet. The sample is mounted on a transparent, low-concentration (0.5%) agarose gel (Figure 1.13). This agarose is prepared from an aqueous solution adequate for the sample, in our case, phosphate buffered saline (PBS), providing a suitable environment for a live sample. The cylinder of agarose containing the sample is immersed in PBS, which virtually eliminates refractive imaging artifacts at the agarose surface. The cylinder containing the sample is supported from above by a micropositioning device. By using the four available degrees of freedom (three translational and one rotational), the sample can be positioned such that the excitation light illuminates the plane of interest. An objective lens, detection filter, and tube lens are used to image the distribution of fluorophores in the illumination plane onto a CCD camera, with the detection axis arranged perpendicular to the axis of illumination. The light sheet thickness is adapted to the detection lens, i. e. the light sheet is made as thin as possible while keeping it uniform across the complete FOV of the objective lens. Its thickness is typically between 3 and 10 μm; e. g. for a 10×, 0.30 NA objective lens, the light sheet beam waist can be reduced to 6 μm, and the resulting width will vary less than 42% across the FOV of 660 μm.

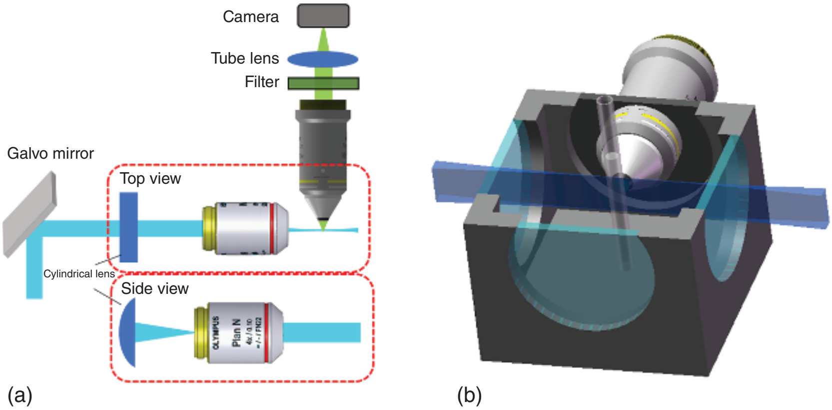

Figure 1.13 Light sheet with cylinder lens. (a) Top view and side view of illumination path. (b) 3D diagram of a typical sample pool. Source: Chong Chen.

Any fluorescence imaging system suffers from scattering and absorption in the tissue; in large and highly scattering samples, the image quality decreases as the optical path length in the sample increases. This problem can be reduced by multiview reconstruction, in which multiple 3D data sets of the same object are collected from different directions and combined in a postprocessing step. The sample was rotated mechanically and for each orientation (0°, 90°, 180°, and 270°) a stack was recorded. The stacks were then reoriented in the computer to align them with the stack recorded at 0°. The fusion of these four data stacks yields a superior representation featuring similar clarity and resolution throughout the entire specimen.

1.4.2.2 Scanning Light Sheet

As known, the Gauss beam intensity is nonuniform. A digital scanned laser light sheet fluorescence microscopy (DSLM) was developed to achieve the imaging speed and quality required for recording large specimen [32]. (Figure 1.14) The idea behind DSLM is to generate a “plane of light” with a laser scanner that rapidly moves a micrometer-thin beam of laser light vertically and horizontally through the specimen. The DSLM has several advantages over standard light sheet microscopy. First, DSLM illuminates each line in the specimen with the same intensity, a crucial prerequisite for quantitative imaging of large specimens. Second, in contrast to standard light sheet-based microscopy, DSLM does not rely on apertures to form the laser profile, which reduces optical aberrations and thereby provides an exceptional image quality. Third, the entire illumination power of the light source is focused onto a single line, resulting in an illumination efficiency of 95% as compared with 3% in standard light sheet microscopy. Fourth, DSLM allows generating intensity-modulated illumination patterns (structured illumination), which can be used to enhance the image contrast in highly light-scattering specimens, such as large embryos.

One of the fundamental novel ideas of the DSLM concept is the use of laser scanners to create a 2D sample illumination profile perpendicular to the detection axis. In the standard mode of DSLM operation, one of the scan mirrors of the scan

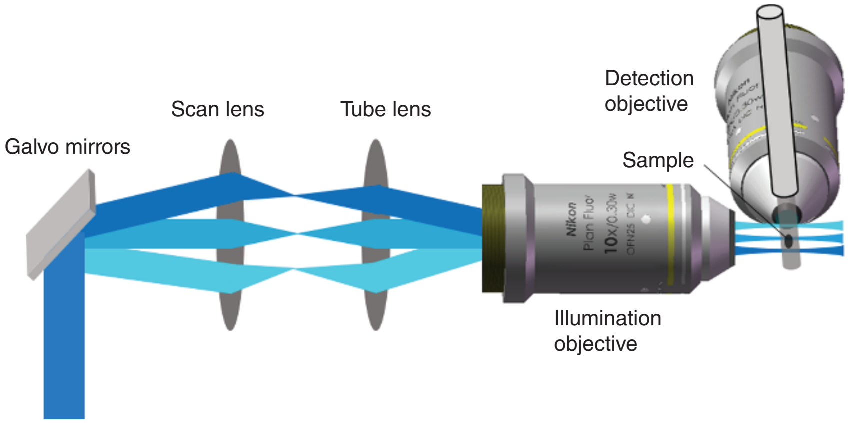

Figure 1.14 Light sheet with scanning beams. (a) Gaussian beam. (b) Bessel beam. Source: Chong Chen.

head moves at a constant speed within a predefined angular range. An f-theta lens converts the angular scan range of the laser beam into a vertical set of parallel beams. Because of the scanning approach, a single diffraction-limited beam of light illuminates the sample at any time point along a well-defined line in space. Integration over time and space results in the illumination of an entire plane. Thus, in order to obtain a two-dimensional image, the camera integrates the signal while the laser scanners illuminate the respective plane in the detection system's FOV. By using a constant scan speed, a homogeneous light sheet-like profile is generated, i.e. all horizontal lines are illuminated with the same light intensity. Because of the high scan speed, the entire two-dimensional profile is created in less than 1 ms, regardless of the extent of the field-of-view. The complete DSLM illumination/excitation system (subsystems 1–3 above) consists e.g. of a multiline argon krypton laser, an AOTF for laser wavelength selection and intensity control, a two-axis high-speed scan head, an f-theta lens, and a low-NA illumination objective lens operated with a regular tube lens. The illumination/excitation objective lens is mounted on a piezo nanofocus, which can move the lens along its optical axis. The specimen is placed inside a custom specimen chamber made e.g. from inert black Delrin. The specimen chamber features a temperature control system, which includes a temperature sensor inside the chamber and a heating foil attached below the chamber [33, 34].

1.4.2.3 Multidirection Illumination and Imaging

The SiMView microscope for one-photon excitation consists of custom laser light sources, two scanned light-sheet illumination arms, two fluorescence detection arms equipped with sCMOS cameras, a custom four-view specimen chamber with perfusion system, and a four-axis specimen positioning system that is magnetically connected to the specimen holder in the imaging chamber (Figure 1.15) [35–38].

The four-view specimen chamber comprises a custom specimen holder, a custom mechanical scaffold manufactured from black Delrin, a multistage adaptor module for connecting the specimen holder to the specimen positioning, system and a custom perfusion system. The specimen holder was produced from medical-grade stainless steel. Using the positioning system, the holder can be translated in three dimensions and rotated around its main axis without breaking the water seal.

Although this has been successful for imaging large multicellular organisms at single-cell resolution, a tradeoff exists between the minimum thickness of the light sheet and the FOV over which it remains reasonably uniform, such that, when imaging a 50-μm-diameter cultured cell, an optimized Gaussian light sheet diverges to a full-width at half-maximum (FWHM) thickness of 2.8 μm at either end. However, such light sheets are too thick to aid in improving axial resolution, which is 3–4 times poorer than transverse resolution, even when high-NA optics are used. To generate much thinner light sheets, the bessel beams are created by projecting an annular illumination pattern at the rear pupil of an excitation lens. Their central peak width, unlike Gaussian beams, can be decoupled from their longitudinal extent simply by changing the thickness of the annulus. The self-reconstructing property of such beams has recently been used to reduce shadowing and scattering artifacts

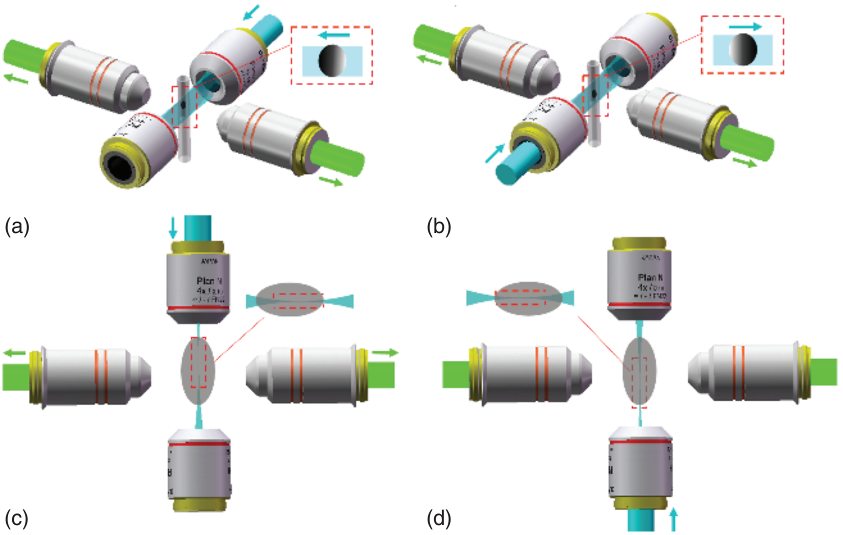

Figure 1.15 Light sheet with multi-direction illumination and detection. (a, b) Schematic of two directions of light sheet illumination, respectively. (c, d) Top view of a and b. Source: Chong Chen.

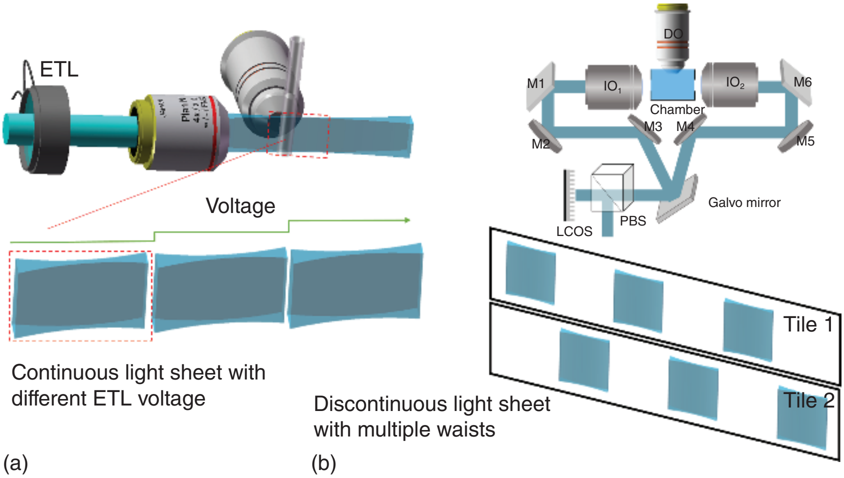

Figure 1.16 Light sheet microscope for extended field of view. (a) Schematic of light sheet microscopy for extended field of view with ETL; (b) Schematic of light sheet microscopy for extended field of view with LCOS (liquid crystal on silicon). Source: Chong Chen.

in plane illumination microscopy of multicellular organisms. Eric Betzig et al. use scanned Bessel beams of higher NA to create light sheets sufficiently thin to achieve isotropic 3D resolution and improve the expenditure of the photon budget to the point at which hundreds of 3D image stacks comprising tens of thousands of frames can be acquired from single living cells at rates of nearly 200 frames/s.

In order to improve the 3D imaging ability of SPIM on large specimens, tremendous efforts have been spent on the optimization of the light sheet intensity profile, so that the excitation light can be confined near the detection focal plane over a long distance as much as possible. Unfortunately, the diffraction of light makes it impossible to optimize these properties at the same time. The excitation light is less confined as the length of a light sheet increases, which makes it challenging to image large specimens at high spatial resolutions using SPIM. One of the most effective approaches is to quickly move the light sheet axially within the imaging plane along the excitation light propagation direction, so that a high spatial resolution and good optical sectioning ability can be maintained in a FOV much larger than the size of the light sheet. Tiling light sheet selective plane illumination microscopy (TLS-SPIM) is a method using this strategy to improve the 3D imaging ability of SPIM on large specimens. In TLS-SPIM, a large FOV is imaged by tiling a short but thin light sheet at multiple positions within the imaging plane and taking an image at each light sheet tiling position (Figure 1.16).

Scanning coaxial beam arrays, which are often created by diffraction optical elements (DOEs), can produce discontinuous light sheets. However, a DOE element only generates a coaxial beam array with a fixed intensity profile, which reduces the flexibility of TLS-SPIM. Additionally, the binary SLM included in common TLS microscopes can produce coaxial beam arrays so that the microscope has the ability to use with different intensity profiles, beam numbers, and periods. DOEs could be used in two ways in TLS-SPIM for 3D imaging. First, the imaging plane can be imaged by tiling the same DOE at multiple positions, which is the same as the operation in regular TLS-SPIM. Second, the imaging plane can be imaged by using multiple different DOEs with light sheet waists compensating for each other. The Galvo mirror directs the illumination light to one of the two symmetrical illumination paths by offsetting the initial angle and creates a virtual excitation light sheet for sample illumination by scanning the laser beam [39].

1.4.3 Single-Lens Light-Sheet Microscopy

The potential drawback of SPIM is that it requires the sample to be illuminated with a lens that is in the plane of the sample being imaged, and this means that conventional sample preparation techniques, e.g. glass microscope slides, cannot be used [3]. Recently, highly inclined laminated optical sheet microscopy was discovered to illuminate a thin sheet in a sample using the same objective that is used to collect the fluorescence [40]. The approach is similar to SPIM but with two significant differences: the illumination and detection beams are not at 90° (as is usual for SPIM) and the sheet of illumination does not align in the focal plane of the imaging system used to collect the reflected/scattered light or fluorescence (Figure 1.17).

Oblique plane microscopy (OPM) shows that a similar concept can be applied to HiLo/SPIM, where the third microscope is used to tilt the image plane, rather than using it to image planes located at different axial positions. Thus, in-focus imaging of an oblique plane within the specimen is achieved. By taking advantage of the fact that high numerical aperture (NA) microscope objectives have an angular extent

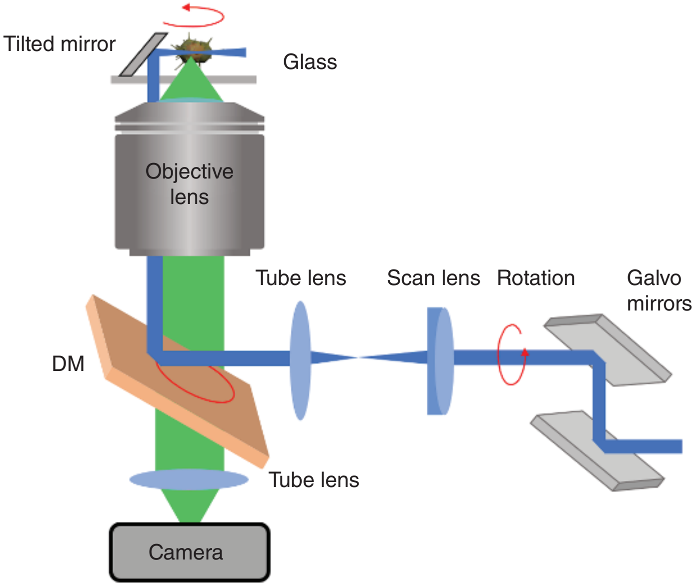

Figure 1.17 Light sheet with a single objective. Source: Chong Chen.

that is much larger than 90°. In order to create an oblique sheet of illumination within the specimen, the laser beam was first expanded using a 10× telescope. As shown in Figure 1.18, the light was then focused by a cylindrical lens onto mirror, M1 and directed to the sample via tube lens 1, a DM and the high numerical aperture objective lens objective lens 1. Mirror M1 allowed the angle of the oblique sheet illumination on the specimen to be conveniently adjusted. Fluorescence from the specimen was then collected by the same objective and an intermediate image plane, IP1, was produced by the first infinity corrected microscope formed by lenses L1 and L2. Light at image plane IP1 is then de-magnified by the second infinity corrected microscope formed by objectives 2 and 3. In order to reimage any plane within the specimen, it is necessary to ensure that the lateral and axial magnifications between the specimen and FP3 are equal. This condition is achieved when the magnification is equal to n1/n2, where n1 is the refractive index of the immersion medium of the

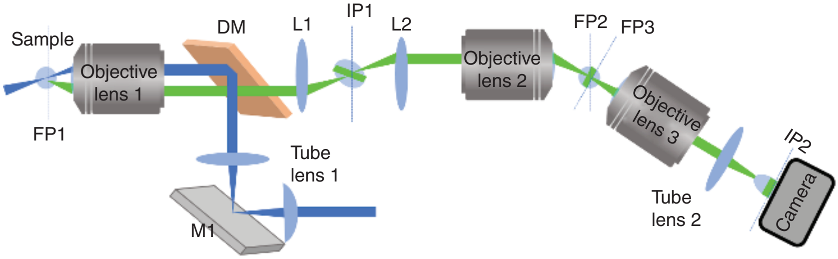

Figure 1.18 Single-lens light sheet illumination with tilt angle corrected. Source: Chong Chen.

specimen and n2 is the refractive index of the immersion medium of the objective lens 2. It was then possible to reimage any plane in the specimen using a third microscope system, which was formed here by objective lenses 3 and tube lens 2.

1.5 Summary

It is very likely that the point-scanning fluorescent microscope and the wide-field fluorescent microscope will coexist in the market for biomedical applications in the near future. However, with the advantages of faster imaging speed and lower photon bleaching, as well as the greatly improved optical sectioning capability and resolution, the wide-field fluorescent microscope may have a wide range of applications, especially for dynamic imaging of live samples, such as live-cell and miniatured model animals. New techniques to further improve their performance are also highly expected.

Nowadays, biomedical studies do not satisfy with the observation of one cell or a few cells. Whole slide or whole sample observation is highly demanded, which requires the optical microscope to have a much bigger FOV without compromising of the resolution. This trend of wide-field fluorescent microscopes has appeared with specially designed objectives and using a camera array for detection.

The other trend of the wide-field fluorescent microscope will be further improvement of the imaging speed, especially for 3D imaging. Currently, the 3D imaging speed is limited by the slow axial translation of the objective or the sample stage. Using an electrical tuning lens to adjust the focus could improve the speed but may introduce additional optical aberration. Simultaneous imaging of multiple planes could be a solution for faster 3D imaging in the future. Introducing adaptive optics to reduce the aberration for thick samples is also highly expected.

With the bigger FOV and faster imaging speed, dramatic amounts of microscope data will be obtained, which are far beyond the capability of human eyes and the current capability of the generally used imaging process software. The development of automatic, precise, and intelligent imaging process algorithms and software will certainly be hot topics for the application of wide-field fluorescent microscopy in modern biomedicine.

References

1 Bauch, H. and Jörg, S. (2006). Optical sections by means of structured illumination: background and application in fluorescence microscopy. *Photonik Int.* 86–88.

2 Dan, D., Yao, B.L., and Lei, M. (2014). Structured illumination microscopy for super-resolution and optical sectioning. *Chin. Sci. Bull.* 59: 1291–1307, https://doi.org/10.1007/s11434-014-0181-1.

3 Dan, D. et al. (2013). DMD-based LED-illumination super-resolution and optical sectioning microscopy. *Sci. Rep.* 3: 1116, https://doi.org/10.1038/srep01116.

4 Xu, D. et al. (2013). Fast optical sectioning obtained by structured illumination microscopy using a digital mirror device. *J. Biomed. Opt.* 18: 060503, https://doi.org/10.1117/1.JBO.18.6.060503.

5 Lin, C.Y., Lin, W.H., Chien, J.H. et al. (2016). In vivo volumetric fluorescence sectioning microscopy with mechanical-scan-free hybrid illumination imaging. *Biomed. Opt. Express* 7: 3968–3978, https://doi.org/10.1364/BOE.7.003968.

6 Yang, X. et al. (2019). Fringe optimization for structured illumination super-resolution microscope with digital micromirror device. *J. Innovative Opt. Health Sci.* 12, https://doi.org/10.1142/s1793545819500147.

7 Poher, V. et al. (2007). Optical sectioning microscopes with no moving parts using a micro-stripe array light emitting diode. *Opt. Express* 15: 11196–11206.

8 Lim, D., Ford, T.N., Chu, K.K., and Metz, J. (2011). Optically sectioned in vivo imaging with speckle illumination HiLo microscopy. *J. Biomed. Opt.* 16: 016014.

9 Hoffman, Z.R. and DiMarzio, C.A. (2013). Structured illumination microscopy using random intensity incoherent reflectance. *J. Biomed. Opt.* 18: 061216, https://doi.org/10.1117/1.JBO.18.6.061216.

10 Neil, M., Juškaitis, R., and Wilson, T. (1997). Method of obtaining optical sectioning by using structured light in a conventional microscope. *Opt. Lett.* 22 (24): 1905–1907.

11 Neil, M., Squire, A., JusĬkaitis, R. et al. (2000). Wide-Ūeld optically sectioning euorescence microscopy with laser illumination. *J. Microsc-Oxford* 197: 1ą4.

12 Ford, T.N., Lim, D., and Mertz, J. (2012). Fast optically sectioned fluorescence HiLo endomicroscopy. *J. Biomed. Opt.* 17: 021105, https://doi.org/10.1117/1.JBO.17.2.021105.

13 O'Holleran, K. and Shaw, M. (2014). Optimized approaches for optical sectioning and resolution enhancement in 2D structured illumination microscopy. *Biomed. Opt. Express* 5: 2580–2590, https://doi.org/10.1364/BOE.5.002580.

14 Zhou, X. et al. (2015). Double-exposure optical sectioning structured illumination microscopy based on Hilbert transform reconstruction. *PLoS One* 10: e0120892, https://doi.org/10.1371/journal.pone.0120892.

15 Gustafsson, M.G. (2000). Surpassing the lateral resolution limit by a factor of two using structured illumination microscopy. *J. Microsc.* 198: 82–87, https://doi.org/10.1046/j.1365-2818.2000.00710.x.

16 Gustafsson, M.G. et al. (2008). Three-dimensional resolution doubling in wide-field fluorescence microscopy by structured illumination. *Biophys. J.* 94: 4957–4970, https://doi.org/10.1529/biophysj.107.120345.

17 Gustafsson, M.G. (2005). Nonlinear structured-illumination microscopy: wide-field fluorescence imaging with theoretically unlimited resolution. *Proc. Natl. Acad. Sci. U.S.A.* 102: 13081–13086, https://doi.org/10.1073/pnas.0406877102.

18 Li, D. et al. (2015). Advanced imaging. Extended-resolution structured illumination imaging of endocytic and cytoskeletal dynamics. *Science* 349: aab3500, https://doi.org/10.1126/science.aab3500.

19 Schermelleh, L. et al. (2008). Subdiffraction multicolor imaging of the nuclear periphery with 3D structured illumination microscopy. *Science* 320: 1332–1336, https://doi.org/10.1126/science.1156947.

20 Shao, L., Kner, P., Rego, E.H., and Gustafsson, M.G. (2011). Super-resolution 3D microscopy of live whole cells using structured illumination. *Nat. Methods* 8: 1044–1046, https://doi.org/10.1038/nmeth.1734.

21 Fiolka, R., Shao, L., Rego, E.H. et al. (2012). Time-lapse two-color 3D imaging of live cells with doubled resolution using structured illumination. *Proc. Natl. Acad. Sci. U.S.A.* 109: 5311–5315, https://doi.org/10.1073/pnas.1119262109.

22 Lu-Walther, H.W. et al. (2015). fastSIM: a practical implementation of fast structured illumination microscopy. *Methods Appl. Fluoresc.* 3: 014001, https://doi.org/10.1088/2050-6120/3/1/014001.

23 Demmerle, J. et al. (2017). Strategic and practical guidelines for successful structured illumination microscopy. *Nat. Protoc.* 12: 988–1010, https://doi.org/10.1038/nprot.2017.019.

24 Forster, R., Wicker, K., Muller, W. et al. (2016). Motion artefact detection in structured illumination microscopy for live cell imaging. *Opt. Express* 24: 22121–22134, https://doi.org/10.1364/OE.24.022121.

25 Lahrberg, M., Singh, M., Khare, K., and Ahluwalia, B.S. (2018). Accurate estimation of the illumination pattern’s orientation and wavelength in sinusoidal structured illumination microscopy. *Appl. Opt.* 57: 1019–1025, https://doi.org/10.1364/AO.57.001019.

26 Forster, R., Muller, W., Richter, R., and Heintzmann, R. (2018). Automated distinction of shearing and distortion artefacts in structured illumination microscopy. *Opt. Express* 26: 20680–20694, https://doi.org/10.1364/OE.26.020680.

27 Perez, V., Chang, B.J., and Stelzer, E.H. (2016). Optimal 2D-SIM reconstruction by two filtering steps with Richardson-Lucy deconvolution. *Sci. Rep.* 6: 37149, https://doi.org/10.1038/srep37149.

28 Huang, X. et al. (2018). Fast, long-term, super-resolution imaging with Hessian structured illumination microscopy. *Nat. Biotechnol.* 36: 451–459, https://doi.org/10.1038/nbt.4115.

29 Voie, A.H., Burns, D., and Spelman, F. (1993). Orthogonal-plane fluorescence optical sectioning: three-dimensional imaging of macroscopic biological specimens. *J. Microsc-Oxford* 170: 229–236.

30 Stelzer, E.H.K. and Lindek, S. (1994). Fundamental reduction of the observation volume in far-field light microscopy by detection orthogonal to the illumination axis: confocal theta microscopy. *Opt. Commun.* 111: 536–547.

31 Haar, F.-M., Swoger, J., and Stelzer, E. (1999). *Developments and Applications of Confocal Theta Microscopy*, vol. 3605 PWB. SPIE.

32 Keller, P.J., Schmidt, A.D., Wittbrodt, J., and Stelzer, E.H. (2008). Reconstruction of zebrafish early embryonic development by scanned light sheet microscopy. *Science* 322: 1065–1069, https://doi.org/10.1126/science.1162493.

33 Planchon, T.A. et al. (2011). Rapid three-dimensional isotropic imaging of living cells using Bessel beam plane illumination. *Nat. Methods* 8: 417–423, https://doi.org/10.1038/nmeth.1586.

34 Fahrbach, F.O., Voigt, F.F., Schmid, B. et al. (2013). Rapid 3D light-sheet microscopy with a tunable lens. *Opt. Express* 21: 21010–21026, https://doi.org/10.1364/OE.21.021010.

35 Ahrens, M.B., Orger, M.B., Robson, D.N. et al. (2013). Whole-brain functional imaging at cellular resolution using light-sheet microscopy. *Nat. Methods* 10: 413–420, https://doi.org/10.1038/nmeth.2434.

36 Voigt, F.F. et al. (2019). The mesoSPIM initiative: open-source light-sheet microscopes for imaging cleared tissue. *Nat. Methods* 16: 1105–1108, https://doi.org/10.1038/s41592-019-0554-0.

37 Wu, Y. et al. (2013). Spatially isotropic four-dimensional imaging with dual-view plane illumination microscopy. *Nat. Biotechnol.* 31: 1032–1038, https://doi.org/10.1038/nbt.2713.

38 Krzic, U., Gunther, S., Saunders, T.E. et al. (2012). Multiview light-sheet microscope for rapid in toto imaging. *Nat. Methods* 9: 730–733, https://doi.org/10.1038/nmeth.2064.

39 Wu, Y. et al. (2017). Reflective imaging improves spatiotemporal resolution and collection efficiency in light sheet microscopy. *Nat. Commun.* 8: 1452, https://doi.org/10.1038/s41467-017-01250-8.

40 Tokunaga, M., Imamoto, N., and Sakata-Sogawa, K. (2008). Highly inclined thin illumination enables clear single-molecule imaging in cells. *Nat. Methods* 5: 159–161, https://doi.org/10.1038/nmeth1171.